



Publication Year	2015
Acceptance in OA @INAF	2020-04-24T13:26:21Z
Title	Star formation properties of sub-mJy radio sources
Authors	Bonzini, M.; Mainieri, V.; Padovani, P.; Andreani, P.; Berta, S.; et al.
DOI	10.1093/mnras/stv1675
Handle	http://hdl.handle.net/20.500.12386/24226
Journal	MONTHLY NOTICES OF THE ROYAL ASTRONOMICAL SOCIETY
Number	453

Star formation properties of sub-mJy radio sources

M. Bonzini,^{1★} V. Mainieri,^{1★} P. Padovani,¹ P. Andreani,¹ S. Berta,² M. Bethermin,¹
D. Lutz,² G. Rodighiero,³ D. Rosario,² P. Tozzi⁴ and S. Vattakunnel⁵

¹European Southern Observatory, Karl-Schwarzschild-Strasse 2, D-85748 Garching, Germany

²Max-Planck-Institut für extraterrestrische Physik, Giessenbachstraße, D-85748 Garching, Germany

³Dipartimento di Fisica e Astronomia, Università di Padova, vicolo dell'Osservatorio 3, I-35122 Padova, Italy

⁴INAF – Osservatorio Astrofisico di Arcetri, Largo E. Fermi, I-50125 Firenze, Italy

⁵INAF – Osservatorio Astronomico di Trieste, via G.B. Tiepolo 11, I-34131 Trieste, Italy

Accepted 2015 July 22. Received 2015 July 7; in original form 2014 June 6

ABSTRACT

We investigate the star formation properties of ~ 800 sources detected in one of the deepest radio surveys at 1.4 GHz. Our sample spans a wide redshift range (~ 0.1 –4) and about four orders of magnitude in star formation rate (SFR). It includes both star-forming galaxies (SFGs) and active galactic nuclei (AGNs), further divided into radio-quiet (RQ) and radio-loud objects. We compare the SFR derived from the far-infrared luminosity, as traced by *Herschel*, with the SFR computed from their radio emission. We find that the radio power is a good SFR tracer not only for pure SFGs but also in the host galaxies of RQ AGNs, with no significant deviation with redshift or specific SFR. Moreover, we quantify the contribution of the starburst activity in the SFG population and the occurrence of AGNs in sources with different level of star formation. Finally, we discuss the possibility of using deep radio survey as a tool to study the cosmic star formation history.

Key words: surveys – galaxies: active – galaxies: starburst – galaxies: star formation – radio continuum: galaxies.

1 INTRODUCTION

The faint radio sky is a complex mixture of star-forming galaxies (SFGs) and active galactic nuclei (AGNs; e.g. Mauch & Sadler 2007; Smolčić et al. 2008; Padovani et al. 2009, 2011). Indeed, radio emission can either be due to the relativistic jets powered by the AGN or to synchrotron emission from electrons accelerated by supernova (SN) explosions. In the latter case, radio emission can then be used as a star formation rate (SFR) tracer (e.g. Yun, Reddy & Condon 2001; Pannella et al. 2009) which opens the possibility of using radio survey to study the cosmic star formation history (CSFH). Moreover, the radio band has the advantage, compared to UV or optical frequencies, to offer a dust unbiased estimate of the SFR being almost unaffected by dust extinction.

However, the majority of radio surveys available up to now were only sensitive to the most powerful radio-loud (RL) AGNs, whose radio emission is mainly due to the relativistic jets rather than to star formation (SF). In the few cases in which the sensitivity was high enough to detect SFGs, only the most extreme starburst (SB) galaxies, with SFRs $\gtrsim 1000 M_{\odot} \text{ yr}^{-1}$, could be detected above redshift about 1, at the mJy level. It is only going below 0.1 mJy, that we become sensitive, over a wider redshift range, to the bulk

of the SFG population, which moreover represents the dominant contribution to the overall radio population at these radio flux densities (e.g. Padovani et al. 2011, 2015; Bonzini et al. 2013). Such a sensitivity has been reached so far only on small patches of the sky as with the Very Large Array (VLA) survey of the Extended *Chandra Deep Field-South* (E-CDFS) considered in this work.

A further problem that has limited so far the use of radio surveys for studying the CSFH is the challenge of separating the two radio emission mechanisms, jets and SF, in faint radio samples. In particular, the origin of radio emission in the so-called radio-quiet (RQ) AGNs has been a matter of debate for quite some time. It has been proposed that these sources are a scaled-down version of RL objects (e.g. Miller, Rawlings & Saunders 1993; Giroletti & Panessa 2009) or that the radio emission is mostly due to the SF in the host galaxy (e.g. Sopp & Alexander 1991). In the former case, the SFR derived from the radio power would be overestimated compared to the one obtained by other SFR tracers like, for example, the far-infrared (FIR) luminosity.

If instead radio emission in RQ AGNs is due to SF, the radio power could be used as an SFR tracer even when the AGN emission strongly contaminates the optical-to-MIR host galaxy light. This would allow us to include powerful AGN hosts in SFR studies, therefore superseding the limitation of many current works that are restricted to pure star-forming systems. However, it is first necessary to find an effective method to separate RQ and RL AGNs, as in the

* E-mail: marghe.bonzini@gmail.com (MB); vmainier@eso.org (VM)

latter sources the radio luminosity primarily traces the jet emission. In Bonzini et al. (2013) we have proposed a method to separate these two AGN populations. We note that the RL AGN contribution to the CSFH is expected to be low for two main reasons; first, RL AGNs represent only a small fraction (10 per cent) of the radio sources at flux densities of $\sim 30 \mu\text{Jy}$ and, secondly, their host galaxies have usually low SFRs as they are mainly passive systems.

Moreover, estimating the SF activity in AGNs host galaxies is particularly important to investigate the possible impact of the AGN in shaping its host galaxy properties. Indeed, both from the theoretical and observational side, there has been a lot of debate on the role the AGN can have in regulating the SF activity, either triggering or suppressing it (e.g. Harrison et al. 2012; Mullaney et al. 2012; Page et al. 2012; Rosario et al. 2012; Zubovas et al. 2013).

In this work, we exploit the SF properties of a large sample of radio sources selected in a deep VLA survey of the E-CDFS down to a 5σ flux density limit of about $32 \mu\text{Jy}$. The paper is organized as follows. In Section 2 we described our radio sample, how it splits into the different source populations, and the ancillary data used for the analysis. After describing the method adopted to estimate the FIR luminosity of the radio sources (Section 3), we present the radio–FIR correlation (RFC) for radio selected SFGs (Section 4). In Section 5 we compute the SFR from the radio and FIR luminosity, and we compare them in Section 6. The position of our radio selected sources in the SFR–stellar mass plane is described in Section 7, and in Section 8 their SF activity is investigated. In Sections 9 and 10, we discuss and summarize our results, respectively. Finally, Appendix A is dedicated to the description of the empirical model we compare with our observations and in Appendix B we describe the catalogue with the physical properties of the radio sources used in this work that we make publicly available.

In this paper, we assume a cosmology with $H_0 = 70 \text{ km s}^{-1} \text{ Mpc}^{-1}$, $\Omega_M = 0.27$, and $\Omega_\Lambda = 0.73$ and a Chabrier initial mass function (IMF; Chabrier 2003).

2 SAMPLE DESCRIPTION

2.1 Radio data

The E-CDFS has been observed with the VLA at 1.4 GHz between 2007 June and September (Miller et al. 2008). The survey reaches a best rms sensitivity of $6 \mu\text{Jy}$ and the average 5σ flux density limit is $37 \mu\text{Jy}$ with near-uniform coverage. A catalogue including sources down to peak flux density of five times the local rms noise has been extracted. A description of the survey strategy and the data reduction details are given in Miller et al. (2013). The radio catalogue includes 883 sources. Using a likelihood ratio technique (Ciliegi et al. 2003), the optical/infrared counterparts of the radio sources have been identified (Bonzini et al. 2012). Excluding the outermost region as defined in Bonzini et al. (2012), the wealth of multiwavelength data available for the E-CDFS allows robust estimates of photometric redshifts (Santini et al. 2009; Taylor et al. 2009; Cardamone et al. 2010; Rafferty et al. 2011). The area with photometric redshifts coverage includes 779 radio sources that will constitute our main sample for the analysis presented in this paper. Combining the photometric redshifts with the output of several spectroscopic campaign in the E-CDFS, we were able to assign a redshift to a total of 675 radio sources, 37 per cent of which are spectroscopic (see Bonzini et al. 2012, for details). The average redshift is $\langle z \rangle \sim 1.1$.

2.2 Radio source populations

As mentioned in Section 1, the sub-mJy radio population is a mixture of SFG and AGN. The latter further divides into RQ and RL AGN. To separate these different populations, we use a multiwavelength approach combining radio, mid-infrared (MIR), and X-ray data. A detailed description of our classification scheme is given in Bonzini et al. (2013); here we briefly summarize its main characteristics. We select RL AGN using the $q_{24\text{obs}}$ parameter, which is the logarithm of the ratio between the observed $24 \mu\text{m}$ flux density and the observed 1.4 GHz flux density (e.g. Sargent et al. 2010, and references therein). In the $q_{24\text{obs}}$ –redshift plane, we have defined an ‘SFG locus’ below which we find radio sources with a radio excess compared to the typical $q_{24\text{obs}}$ ratio of SF systems. This excess is the signature of an AGN contribution to the radio luminosity; these sources have been referred to as radio-dominant AGNs (Appleton et al. 2004), radio-excess AGNs (e.g. Drake et al. 2003; Del Moro et al. 2013), or simply RL AGNs (e.g. Donley et al. 2005; Padovani et al. 2009) in the literature. Here, we adopt the nomenclature RL AGNs. The SFG locus has been obtained computing the $q_{24\text{obs}}$ as a function of redshift for the SFG M82 (Polletta et al. 2007) and assuming a 0.7 dex dispersion. In Bonzini et al. (2013) we have discussed the implications of choosing the M82 template for source classification (see also Section 6). Within and above this locus, both SFGs and RQ AGNs can be found (e.g. Donley et al. 2005; Bonzini et al. 2013). A source is classified as RQ AGN if there is any evidence of AGN activity in the other bands considered: we classify a radio source as RQ AGN if (a) it has a hard band [2–10 keV] X-ray luminosity greater than $10^{42} \text{ erg s}^{-1}$; (b) it lies in the ‘AGN wedge’ of the IRAC colour–colour diagram, as defined by Donley et al. (2012). Otherwise, the object is classified as an SFG. According to this scheme, our sample of 779 radio sources includes 167 RL AGNs, 188 RQ AGNs, and 424 SFGs.

2.3 Herschel data

The E-CDFS has been observed by *Herschel* as part of the PEP (PACS Evolutionary Probe) programme (Lutz et al. 2011). The *Herschel* observations are deeper in the central part of the field, the Great Observatories Origins Deep Survey (GOODS) field, and shallower in the outskirts. The whole field has been observed at 100 and $160 \mu\text{m}$ and for the central part $70 \mu\text{m}$ data are also available. For GOODS proper, we use the combined reduction of PEP and GOODS–*Herschel* (Elbaz et al. 2011) Photodetector Array Camera and Spectrometer (PACS) data as described in Magnelli et al. (2013). The 5σ flux level of the 100 ($160 \mu\text{m}$) maps is 0.85 (2.1) mJy and 6.25 (13.05) mJy in the GOODS and E-CDFS, respectively. The $70 \mu\text{m}$ 5σ flux density limit is 1.35 mJy. *Herschel* photometry was performed through point spread function (PSF) fitting, adopting Multiband Imaging Photometer for *Spitzer* (MIPS) $24 \mu\text{m}$ detected sources as positional priors (Berta et al. 2013). Blind catalogues are also extracted by means of PSF-fitting using the STARFINDER IDL code (Diolaiti et al. 2000a,b) and include all sources with $S/N > 3\sigma$. We cross-correlate this *Herschel*/PACS catalogues with our radio sample using a 1.5 arcsec searching radius. We find a total of 490 matches, 33 per cent in the GOODS field and 67 per cent in the outer region of the E-CDFS.

In particular, in the PACS-radio sub-sample we have 42 RL AGNs, 130 RQ AGNs, and 311 SFGs. We note that in the PACS sample we recover 69 per cent of the RQ AGNs, 78 per cent of the SFGs but only 25 per cent of the RL AGNs from the original radio selected sample considered in this paper. The small fraction of

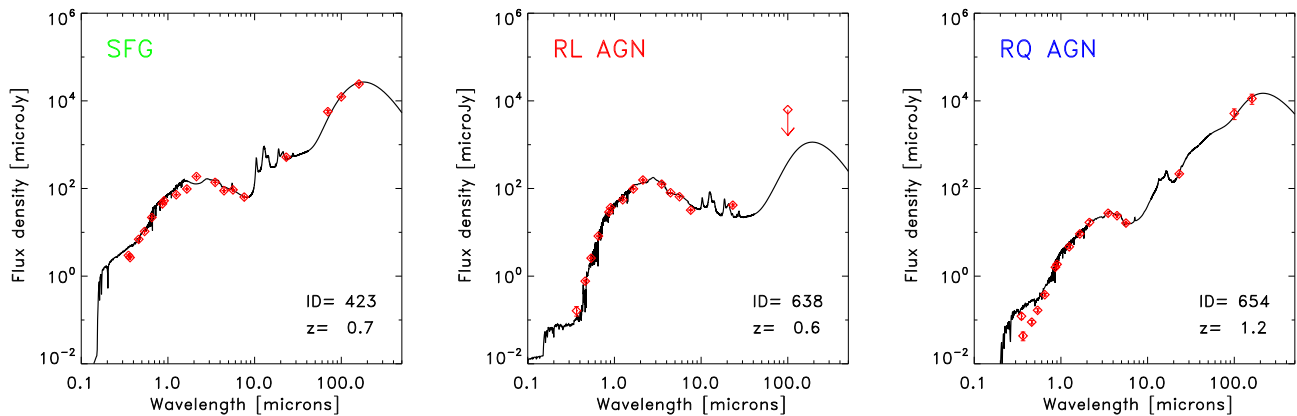


Figure 1. Examples of the optical-to-FIR SED fitting for the three classes of sources. The combined photometry is plotted as red symbols as a function of wavelength (observed frame) and the solid lines show the best-fitting template. Source ID and redshift are given in the bottom-right corner.

RL AGN is not surprising since they are preferentially hosted in passive, dust-poor, galaxies. We therefore expect only a small fraction of them to be detected in the FIR.

For the radio sources without a PACS counterpart, we compute 5σ upper limits from the local rms noise, therefore taking into account the non-uniform coverage of the *Herschel* observations in this field.

3 FIR LUMINOSITY OF RADIO SOURCES

The *Herschel* photometry is crucial to have a good estimate of the FIR emission since it allows us to trace the cold dust emission. At a typical redshift of ~ 1 , the PACS measurements probe the rising part and/or the peak of the rest-frame FIR dust emission bump. We apply a fitting technique to the full UV-to-FIR spectral energy distribution (SED) to better constrain the FIR luminosity of our radio sample, taking advantage of the exquisite multiwavelength coverage available in the E-CDFS.

The UV–NIR photometry is obtained combining the *BVR* selected Cardamone et al. (2010) catalogue, the *K* selected Taylor et al. (2009) catalogue, and the Damen et al. (2011) IRAC selected *Spitzer* IRAC/MUSYC Public Legacy in the *ECDFS* survey (SIMPLE) catalogue. In the MIR, we used the MIPS 24 and 70 μm observations from the Far-Infrared Deep Extragalactic Legacy Survey (FIDEL; Dickinson & FIDEL Team 2007). A likelihood ratio technique (Ciliegi et al. 2003) followed by a careful visual inspection has been used to reconstruct the optical-to-MIR photometry of the radio sources (see Bonzini et al. 2013, for details). At longer wavelengths, given the lower surface density of sources, we simply cross-correlate the *Herschel* and radio counterpart catalogues, as described in the previous section. In the GOODS field, the PACS 70 μm detection rather than the MIPS one is adopted when available. In summary, for each radio source we have on average 16 photometric points.

To fit the UV-to-FIR photometry, we use the Berta et al. (2013) template library that is based on the observed SED of PACS detected sources. It is a collection of 32 templates, mostly SFGs, of which 12 also include an AGN component.

We chose this library mostly for its wide range of SED shapes. This is important if we want to fit the photometry of our radio selected sample since, as already mentioned, it is highly non-homogeneous: it includes both normal SFGs and SB galaxies, objects with the clear presence of a powerful AGN and sources whose SED is dominated at all wavelengths by the emission from stars.

However, as the Berta et al. (2013) library is based on PACS detected sources, it lacks galaxies with very old stellar population and consequently very low emission in the FIR. Therefore, we decided to add three templates of elliptical galaxies from the *Spitzer* Wide-area InfraRed Extragalactic survey (SWIRE) template library (Polletta et al. 2007).

We use a standard χ^2 minimization technique to find the best-fitting template. Examples of the optical-to-FIR SED fitting for the three classes of sources are shown in Fig. 1. For sources without *Spitzer* and/or *Herschel* detections, we imposed the best-fitting template to not exceed the 5σ upper limits in these bands. We finally compute the total FIR luminosity (L_{FIR}) integrating the best-fitting template between 8 and 1000 μm . Errors are computed repeating the fitting procedure 100 times for each source, randomly modifying the photometry within the uncertainties and then taking the standard deviation of the L_{FIR} distribution obtained.

We note that for sources without PACS detection, the FIR luminosity is derived from the best fit based only on the optical–MIR photometry, taking into account the upper limits in the FIR. These luminosity estimates are therefore less robust than the one constrained by the PACS measurements.

4 RADIO–FIR CORRELATION

The radio and FIR luminosity in SFGs follow a tight empirical relation, the so-called radio–FIR correlation (RFC; e.g. Dickey & Salpeter 1984; de Jong et al. 1985; Bell 2003).

The physical reason for its tightness and linearity over several decades in luminosity has been investigated by several theoretical models (e.g. Lacki & Thompson 2010; Lacki, Thompson & Quataert 2010; Schleicher & Beck 2013), but remains still unclear. These works also predict that the RFC should break at high z where inverse Compton losses start to dominate over the non-thermal synchrotron emission.

From the observational point of view, there are some hints of possible deviations at high z or in extreme objects like sub-millimetre galaxies; nevertheless, these observations are still consistent with no significant evolution (e.g. Ivison et al. 2010; Morić et al. 2010; Sargent et al. 2010; Magnelli et al. 2012; Lutz 2014, and reference therein).

Deep radio surveys would be needed to investigate the behaviour of the RFC at high redshift for normal SFGs. Indeed, even to detect SFGs with SFR of hundreds of solar masses per year at $z > 2$, a μJy radio sensitivity is required. Such a sensitivity has been reached so

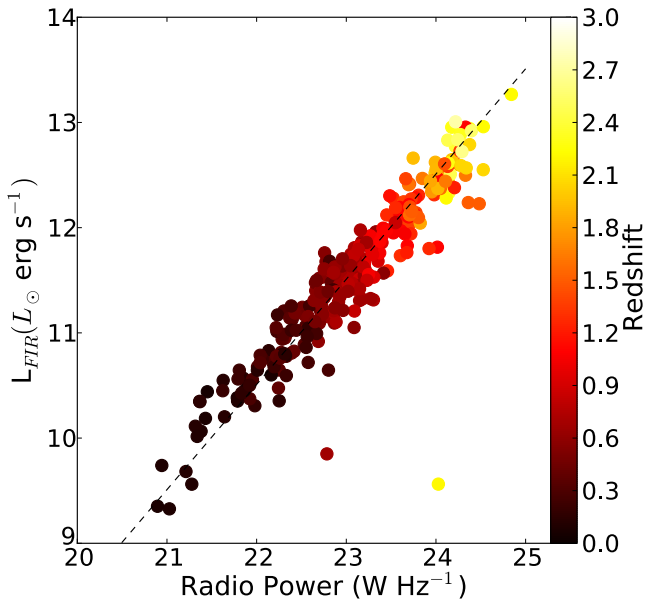


Figure 2. Radio power at 1.4 GHz versus FIR luminosity for SFGs detected by *Herschel*. The colour scale represents the redshift of the sources and the dashed line shows the Kennicutt (1998) relation given in equation (1).

far only for small patches of the sky like in the VLA survey of the E-CDFS considered in this work.

In this section, we therefore investigate the RFC for our radio selected SFGs up to $z \sim 3$. In Fig. 2, we show the radio power versus the FIR luminosity for SFGs with a clear detection in at least one PACS filter since their FIR luminosity estimates are more robust. With the exception of two clear outliers,¹ the two luminosities are tightly correlated and lie along the empirical RFC (e.g. Kennicutt 1998) plotted as dot-dashed line and parametrized by

$$\log(P_{1.4\text{GHz}}) = \log(L_{\text{FIR}}) + 11.47, \quad (1)$$

where $P_{1.4\text{GHz}}$ is the radio power in W Hz^{-1} at 1.4 GHz and L_{FIR} is the FIR luminosity in units of solar luminosity expressed in erg s^{-1} . The average dispersion is 0.2 dex. We note that such a dispersion is smaller compared to the dispersion in $q_{24\text{obs}}$ values for our SFGs that is 0.33 dex. This implies that the correlation between the total FIR luminosity and the radio power is stronger than the one obtained using only MIR data. The colour scale in Fig. 2 represents the redshift of the sources. Thanks to the μJy sensitivity of the VLA observation, we can detect SFGs in a wide redshift range, from $z \sim 0.1$ to $z \sim 3$ and we find that the RFC holds over the whole redshift range with almost constant dispersion. Moreover, our data probe four orders of magnitude in luminosity and therefore include both normal SFGs and the most active systems with SFR of thousands of solar masses per year. The SF in the latter systems is thought to be triggered by episodic violent events such as major mergers rather than by secular processes as in normal SFGs (e.g. Daddi et al. 2010a). Our study suggests that the correlation between

¹ RID 521 (dark point) is a resolved edge-on spiral whose $24 \mu\text{m}$ emission has been probably underestimated due to aperture photometry. As a consequence, the fit is poor and the FIR luminosity is underestimated. RID 577 (light point): there is a small offset between the radio and optical-MIR emission; hence, it is possible that the radio emission is associated with a background object.

radio and FIR emission is the same in both kinds of systems, at least down to the luminosities probed by our observations. However, we still cannot exclude a breakdown at lower SF surface densities as predicted by e.g. Schleicher & Beck (2013) for which even deeper radio data would be needed.

These results justify the use of both the FIR and radio luminosity as independent but equivalent SFR tracers for our radio selected SFGs. It will be a useful element in our investigation on the origin of the radio emission in RQ AGN (see Section 6).

5 SFR ESTIMATE

The FIR luminosity is a tracer of recent SF activity as the UV radiation from young stars is absorbed by the dust and re-emitted at longer wavelengths, in the FIR. The L_{FIR} provides a better estimate of the SFR compared to the one derived from the UV or line emission since these measurements are highly affected by dust extinction. Moreover, computing the SFR from the FIR is particularly useful for bright AGN hosts. Indeed, the AGN emission can overshadow the emission of the whole galaxy at optical wavelength, while it represents a small fraction (< 10 per cent) of the total luminosity in the FIR in most of the cases (e.g. Hatziminaoglou et al. 2010; Rosario et al. 2012; Berta et al. 2013). We adopt the Kennicutt (1998) relation to compute the SFR from the FIR luminosity:

$$\text{SFR}_{\text{FIR}} [\text{M}_{\odot} \text{yr}^{-1}] = 4.5 \times 10^{-44} L_{\text{FIR}} [\text{erg s}^{-1}]. \quad (2)$$

As this equation assumes a Salpeter IMF, we rescaled it for a Chabrier IMF multiplying by a factor of 0.6.

Also the radio continuum emission can be used as a tracer of recent SF in SFGs since it is nearly all due to synchrotron emission from relativistic electrons associated with SN remnants (Condon 1992). The empirical conversion between the radio power at 1.4 GHz and the SFR of the galaxy according to Yun et al. (2001) is

$$\text{SFR}_{\text{r}} [\text{M}_{\odot} \text{yr}^{-1}] = (5.9 \pm 1.8) \times 10^{-22} P_{1.4\text{GHz}} [\text{W Hz}^{-1}]. \quad (3)$$

We multiply the derived SFR by a factor of 0.6 to convert from a Salpeter to a Chabrier IMF.

6 RADIO EMISSION IN RQ AGN

In Fig. 3, we compare the SFR computed from the FIR luminosity with the SFR derived from the radio luminosity for all the 675 radio sources with redshift. Different colours represent different classes of objects: green for SFGs, blue for RQ AGNs, and red for RL AGNs. Sources detected in at least one *Herschel* band are plotted with filled symbols. We first concentrate on these sources since their SFR_{FIR} is more reliable.

As described in Section 4, we find that the SFGs follow the RFC over the whole range in luminosities accessible to our survey. As a consequence, the two SFR estimates are in agreement over four decades in SFR with a typical dispersion of 0.2 dex. More interestingly, we find good agreement between the SFRs derived from the two different tracers also for RQ AGNs with only a slightly larger scatter of 0.23 dex. The results of a linear regression fit (least-squares bisector) are

$$\log(\text{SFR}_{\text{FIR}}) = 0.97 \pm 0.02 \times \log(\text{SFR}_{\text{r}}) + 0.02 \pm 0.04 \quad (4)$$

and

$$\log(\text{SFR}_{\text{FIR}}) = 0.96 \pm 0.05 \times \log(\text{SFR}_{\text{r}}) - 0.09 \pm 0.10 \quad (5)$$

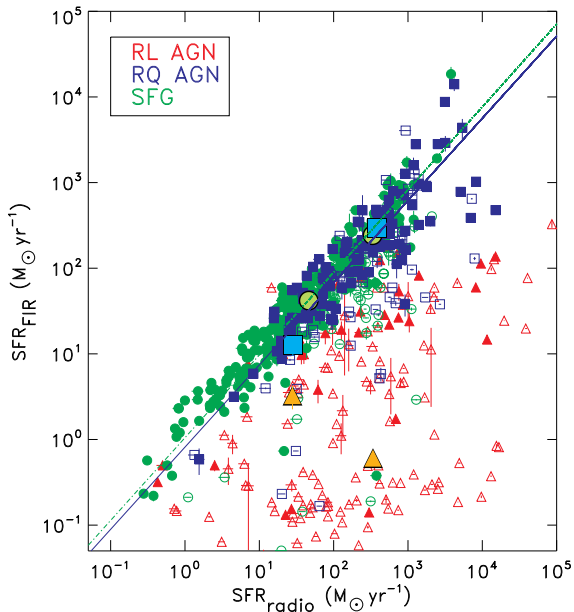


Figure 3. SFR derived from the FIR luminosity versus the SFR from the radio power at 1.4 GHz. SFGs are plotted as green circles, RQ AGNs as blue squares, and RL AGNs as red triangles. Filled symbols represent sources detected in at least one PACS filter, while sources shown as open symbols are *Herschel* non-detections. Large symbols with lighter colours are the results of the stacking analysis (see Section 6.2 for details).

for SFGs and RQ AGNs with PACS detections, respectively. The two relations are fully consistent within the uncertainties. This implies that the radio power is a good tracer for the SFR not only for SFGs, but also for RQ AGNs, with almost the same degree of accuracy for the two types of sources. We emphasize that this result is not a direct consequence of our selection method; indeed, even if both types of sources lie within the ‘SFG locus’ in the $q_{24\text{obs}}$ –redshift plane, they have different MIR characteristics. SFGs, for example, have an average dispersion of $q_{24\text{obs}}$ values of only 0.33 dex while for RQ AGNs the dispersion is two times larger (0.65 dex). This is mainly due to the large AGN contribution at MIR wavelengths in many RQ AGNs. As a consequence, an estimate of the SFR from the observed $24\ \mu\text{m}$ emission would lead to a much more uncertain result for RQ AGNs as for SFGs. Instead, based on Fig. 3, we can claim that the radio luminosity is as good tracer as the FIR of the SF in RQ AGN host galaxies. The correlation shown in Fig. 3 also strongly suggests that the main contribution to the radio emission in RQ AGN is therefore due to the SF in the host galaxy rather than black hole (BH) activity (see also Padovani et al. 2011). As mentioned above, that could not be claimed considering only MIR data as these wavelengths are not reliable for deriving the SFR in many powerful AGNs; it would have been impossible to resolve if the larger scatter in $q_{24\text{obs}}$ values for RQ AGNs compared to SFGs was due to the presence of hot dust heated by the AGNs or to the presence of small radio jets. Hence, it was crucial to include *Herschel* data in our analysis that allowed us to obtain a reliable estimate of the SFR in our sources, assuming that the AGN contribution to the total FIR luminosity is in the large majority of the cases negligible (Hatziminaoglou et al. 2010; Rosario et al. 2012; Berta et al. 2013, see also below).

The behaviour of the RL AGNs further supports our claim that the origin of radio emission in the two types of AGN is different: they scatter out from the one-to-one relation in Fig. 3 since the

SFR computed from the radio luminosity is overestimated due to the jet contribution to the radio power. Note that this is true not only for very powerful RL objects but also for low-power radio AGNs. The comparison of the two SFR tracers allows us also to isolate sources that have been misclassified; indeed, there are some RQ AGNs (~ 5 per cent) with PACS detections that are below the relation, especially at high redshift. In Bonzini et al. (2013), we estimated a contamination to the RQ AGN population from RL AGNs with a strong contribution from the AGN to the $24\ \mu\text{m}$ flux density that boosted their $q_{24\text{obs}}$ value into the SFG locus of about 5 per cent, in agreement with our findings. Therefore, we believe that most of the outliers are indeed RL AGNs.² These outliers are also the main responsible for the slightly larger scatter (0.23 dex) of RQ AGNs as compared to the SFG population (0.2 dex).

6.1 AGN contribution in the FIR

As already mentioned in Section 3, 12 of the SED templates in the library used to fit the photometry of our radio sample include an AGN component. The AGN contribution to the FIR luminosity in these templates has been estimated in Berta et al. (2013). We have therefore the opportunity to subtract the AGN contribution to the SFR_{FIR} and analyse its impact on our conclusions. About 50 per cent of the RQ AGNs and 35 per cent of the SFGs are best fitted by a template that has an AGN component. However, it is important to note that the fit solutions are highly degenerate; in particular, templates with small AGN contribution and pure SFG ones might provide equivalent good fits to the source photometry. Hence, the results reported in the following are valid only in a statistical sense. Nevertheless, the fact that only half of our RQ AGNs are best fitted by an AGN template shows that a classification based only on the optical-to-FIR properties can miss a significant fraction of AGNs. For the latter sources, the AGN contribution to the optical-to-FIR SED is typically minor and, in most of the cases (80 per cent), they are identified as AGNs due to their high X-ray luminosity. On the other hand, the fact that we find some SFGs that are best fitted by an AGN template does not mean that they are all real AGNs. As already highlighted, the SED fitting technique often yields degenerate solutions, especially in the case of discrete libraries. However, it is possible that some of these SFGs are indeed AGNs since our classification scheme was aimed to select a clean sample of RQ AGNs and a contamination from low-luminosity AGNs in the SFG population is expected (see Bonzini et al. 2013, for details).

For all the sources fitted with an AGN template, we subtracted the AGN contribution to the FIR luminosity and re-computed the corresponding SFR. The new best linear regressions have a slope of 0.95 for both SFGs (± 0.02) and RQ AGNs (± 0.05), and the offsets from the 1:1 correlation are 0.04 ± 0.05 and -0.10 ± 0.11 , respectively. They are therefore consistent with the previous estimates within the uncertainties. The only difference is a slightly larger scatter around the best-fitting relation of 0.21 and 0.25 dex for SFGs and RQ AGNs, respectively.

We conclude that the AGN contribution to the FIR emission as computed from the best-fitting template has negligible impact on our results. We will therefore consider the SFR_{FIR} non-corrected for AGN contribution in the rest of this paper.

² We will keep the original classification in the rest of the paper. Nevertheless, we checked if our conclusions change reclassifying these sources, finding no significant differences.

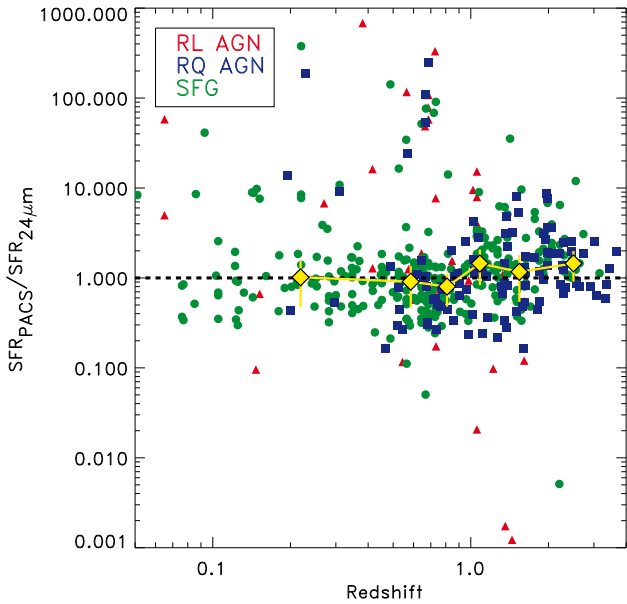


Figure 4. Ratio of the SFR computed from the fit to the whole photometry and the one obtained using only the UV-to-24 μm data as a function of redshift. Different colours correspond to different classes of sources as in Fig. 3. Large yellow diamonds represent the median and the standard deviation in different redshift bins.

6.2 Stacking of *Herschel* undetected sources

As already discussed above, for sources without a PACS detection the estimate of the FIR luminosity is less robust. Indeed, the best-fitting template has been obtained considering the photometry only up to 24 μm , with upper limits at longer wavelengths. To estimate how this can impact the SFR estimate, we have re-computed, with the same method, the SFR for sources *with* PACS detection but considering only their photometry up to 24 μm . In Fig. 4, we plot the ratio of the two SFR measurements, considering or not the PACS data, as a function of redshift. Large yellow symbols represent the median and the standard deviation in different redshift bins. We observe a large number of outliers (~ 25 percent) and a slight tendency to underestimate the FIR emission especially above $z \sim 1$ (~ 0.16 dex) when the *Herschel* data are not included in the fitting procedure.

This test explains the larger scatter of the open symbols in Fig. 3 and justifies their exclusion from the linear regression analysis. However, it could be that the good agreement we find between the two SFR tracers holds only for the FIR-brightest objects while it breaks for the *Herschel* undetected sources.

Therefore, we performed a mean stacking analysis (B  thermin et al. 2010) of the PACS-undetected sources to estimate their average SFR_{FIR} . We divide the undetected sources into classes, and for each class we split the sample into two bins of radio power ($21.5 < P_r < 23.5$ and $23.5 < P_r < 24.5$). We then stacked both the 100 and 160 μm *Herschel* maps at the position of the PACS-undetected radio sources using the error maps (Lutz et al. 2011) as weights. Flux densities are extracted from the stacked images through PSF-fitting; aperture corrections and correlated noise corrections are applied (Berta et al. 2013). Uncertainties are estimated using a bootstrap approach (B  thermin et al. 2010) and corrected also for high-pass filtering effects. Table 1 summarizes the stacking analysis results. We obtain $>2\sigma$ detections for SFGs and RQ AGNs in both bands in each bin, with the only exception of the

100 μm stacked image for RQ AGNs in the lower radio power bin. We note that this bin also has the smallest number of sources (12) and therefore the S/N ratio is lower. RL AGNs are detected only at 100 μm in the low radio power bin while they are undetected ($<2\sigma$) elsewhere.

To compute the average FIR luminosity for each sub-sample of sources, we build their average optical-to-FIR SED and then we proceed as described in Section 3. Stacked flux densities below the 2σ threshold are treated as upper limits in the fitting procedure.

The corresponding average SFR_{FIR} are plotted in Fig. 3 as large filled symbols, with colours slightly lighter than the ones of their corresponding source class. The average SFR_{FIR} of PACS-undetected SFGs and RQ AGNs lie within the scatter of the corresponding linear relations. We can therefore conclude that the two SFR tracers are equivalent for our populations of RQ AGNs and SFGs regardless of their IR brightness.

The average SFR_{FIR} of the RL AGNs not detected by *Herschel* (the majority of the population) has been derived taking into account the upper limits obtained with the stacking technique in the PACS bands. Those average values are significantly smaller than the average SFR_r obtained using the mean radio power in each bin. This confirms that their radio luminosity has a significant contribution from the jets and therefore cannot be used to estimate their SFR. We also note that, in both low- and high-power sources, RL AGNs have lower SFR_{FIR} compared to the other two classes of sources meaning that the host galaxies of RL AGNs are on average more passive.

7 SFR VERSUS STELLAR MASS

The SF activity of a galaxy can occur in two different modes (e.g. Daddi et al. 2010b; Genzel et al. 2010): an SB one, probably triggered by major mergers or in dense SF regions; and a quiescent one, associated with secular processes, which is observed in the majority of the SFGs. In this second mode, the SFR is correlated with the stellar mass of the galaxy, forming the so-called main sequence (MS) of SFGs. The MS has nearly the same slope both at low and high redshift but the normalization increases about a factor of 20 from the local Universe to $z \approx 2$ (e.g. Daddi et al. 2007; Elbaz et al. 2007; Noeske et al. 2007; Pannella et al. 2009; Peng et al. 2010; Rodighiero et al. 2011; Wuyts et al. 2011).

In this framework, it is then interesting to locate our sources on the SFR–stellar mass plane. In Fig. 5, we plot the SFR_{FIR} as a function of the galaxy stellar mass for our objects divided into four redshift bins. Having already verified that the radio and the FIR luminosities are equivalently good tracers of the SFR for our SFGs and RQ AGNs, we decided to use in the following the SFR derived from the FIR luminosity because it allows us to carry on the analysis also for RL AGNs for which the SFR_r would instead be meaningless. Moreover, since the SFR_{FIR} is most widely used in the literature, it makes easier the comparisons with previous studies. Stellar masses are computed using a two-component (AGN+galaxy) optical-to-MIR SED fitting technique as described in Bonzini et al. (2013), assuming a Chabrier IMF.

The horizontal dotted line in each panel³ of Fig. 5 marks the minimum SFR (SFR_{min}) accessible to our survey, i.e. the SFR that corresponds to the flux density limit of the VLA observations at the minimum redshift in the specified bin, based on equation (3) and corrected for a Chabrier IMF. Note that SFGs and RQ AGNs

³ In the first redshift bin, the minimum SFR is $0.07 M_{\odot} \text{ yr}^{-1}$.

Table 1. Results of the stacking analysis.

(1)	(2)	(3)	(4)	(5)	(6)	(7)	(8)
Class	No. of sources	Mean z	Mean $P_{\text{R}(1.4\text{GHz})}$ [log (W Hz $^{-1}$)]	$f_{100\ \mu\text{m}}$ (mJy)	$f_{160\ \mu\text{m}}$ (mJy)	$S/N_{100\ \mu\text{m}}$	$S/N_{160\ \mu\text{m}}$
SFG	21	0.86	23.12	7.78	12.90	2.9	2.7
SFG	41	1.88	23.98	2.39	8.08	3.6	2.9
RQ AGN	12	0.68	22.90	1.49	6.48	1.7	4.2
RQ AGN	24	2.03	24.04	4.88	11.10	2.9	2.4
RL AGN	49	0.57	22.90	1.66	3.04	2.6	1.9
RL AGN	37	1.25	23.98	1.09	2.85	1.3	1.4

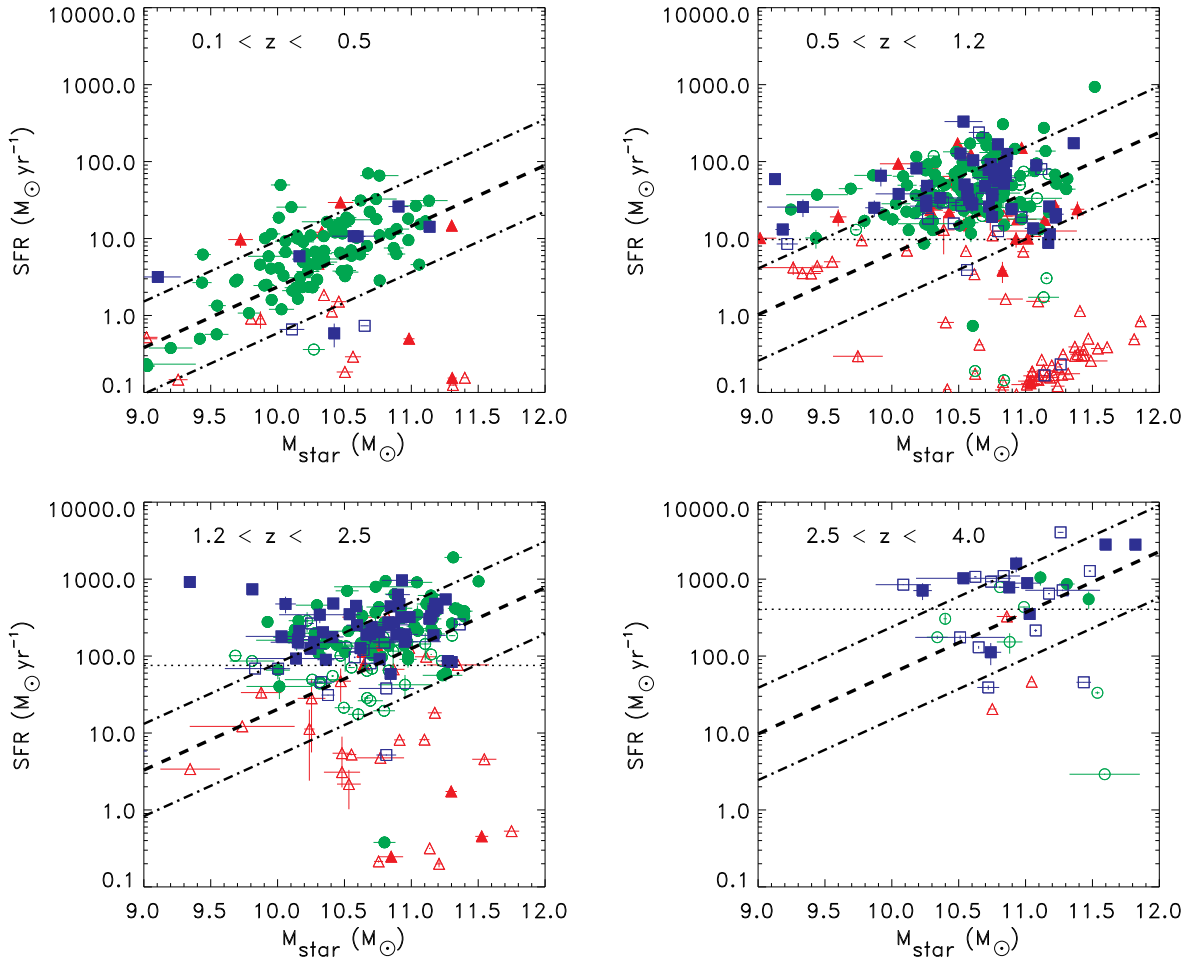


Figure 5. SFR versus stellar mass for different redshift bins. The symbols are the same as in Fig. 3. The horizontal dotted line marks the minimum SFR accessible to our survey in each redshift bin (see the text for details). The dashed line indicates the position of the MS at the average redshift of the sources in each panel. The loci of SB and passive galaxies are delimited by the dot-dashed lines (± 0.6 dex) above and below the MS, respectively.

mostly lie above these lines, being radio emission in both classes associated with SF-related process. RL AGNs instead are detected even when they have SFRs well below the SFR_{min} since their radio emission is boosted by the presence of the jets.

The dashed line indicates the position of the MS at the average redshift of the sources in each bin. We adopt the following law for the redshift evolution of the MS:

$$\log(\text{SFR}(M, z)) = -7.77 + 0.79 \log(M) + 2.8 \log(1 + z), \quad (6)$$

where M is the stellar mass expressed in units of solar masses. The slope and the redshift evolution are based on the results of Rodighiero et al. (2011) and the normalization provides the best

agreement with our data (see Appendix A for details) and it is consistent with the normalizations adopted in the literature [Noeske et al. (2007) for the local universe; Elbaz et al. (2007) and Daddi et al. (2007) for $z \sim 1$ and $z \sim 2$, respectively]. The dot-dashed lines above and below the MS correspond to ± 0.6 dex.

Due to our radio flux density limit, we are able to detect MS galaxies with low stellar mass ($M < 10^{10.5} M_{\odot}$) only in the first redshift bin while at higher redshift we probe the bulk of the MS only at the high-mass end.

We note that RQ AGNs occupy the same locus in the M_{star} –SFR plane as SFGs suggesting that the majority of the host galaxies of radio selected RQ AGNs are not significantly different from the

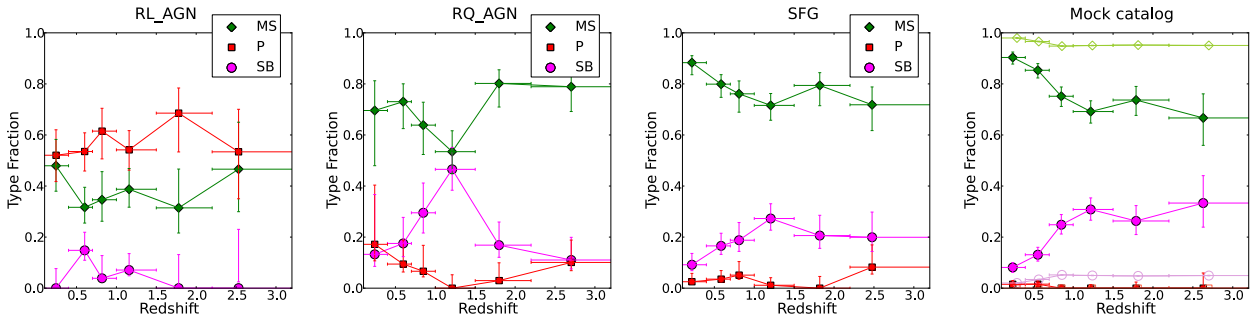


Figure 6. Fraction of SB (magenta circles), MS galaxies (green diamonds), and passive galaxies (red squares) versus redshift. The panels refer from left to right to RL AGNs, RQ AGNs, SFGs, and mock catalogue of star-forming sources. In the latter panel, open (light colours) symbols refer to the mass selected sample, while filled (dark colours) symbols to the mock sample ‘observed’ with the same radio flux density limit of our VLA survey.

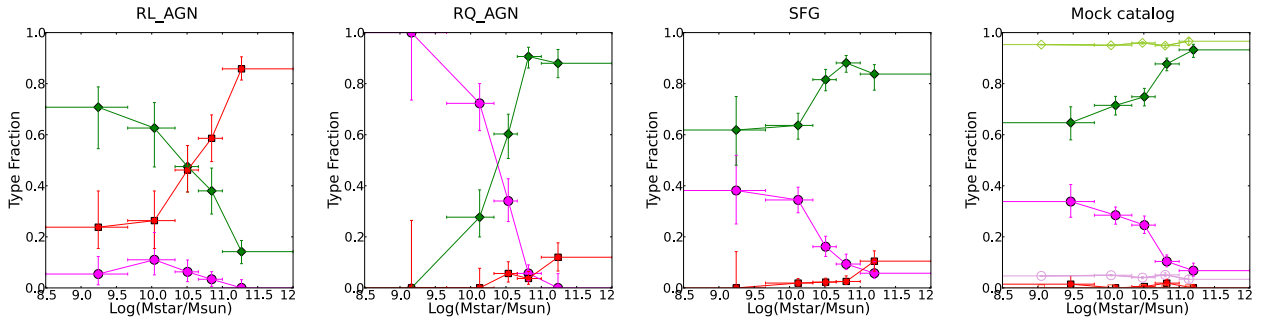


Figure 7. Fraction of SB (magenta), MS galaxies (green), and passive galaxies (red) versus stellar mass. The panels refer from left to right to RL AGNs, RQ AGNs, SFGs, and mock catalogue of star-forming sources. In the latter panel, open (light colours) symbols refer to the mass selected sample, while filled (dark colours) symbols to the mock sample ‘observed’ with the same radio flux density limit of our VLA survey.

inactive galaxy population (see Section 8.3 for a more detailed discussion). The fact that the relative fraction of SFGs over the RQ AGN decreases as a function of redshift is due to a combination of selection and evolutionary effects as further discussed in the next section and in Padovani et al. (2015).

8 SPECIFIC STAR FORMATION RATE

Since the SFR is correlated with the stellar mass, a useful quantity to describe the SF regime of a galaxy is its specific SFR (sSFR), i.e. the SFR divided by the stellar mass. Sources with sSFR particularly higher with respect to the MS are undergoing extremely intense SF activity, possibly triggered by major mergers, while passive galaxies are characterized by very low sSFRs. In this work, we will define as ‘starburst’ those sources whose distance with respect to the MS (i.e. $\Delta \log(\text{sSFR})_{\text{MS}} = \log[\text{sSFR}(\text{galaxy})/\text{sSFR}_{\text{MS}}(M_{\text{star}}, z)]$) is larger than 0.6 dex, and we will call ‘passive galaxies’ those with $\Delta \log(\text{sSFR})_{\text{MS}} < 0.6$ dex (similarly to Rodighiero et al. 2011).

In the following, we will discuss the SF properties of the three classes of sources introduced in Section 2.2. We will treat RL AGNs separately as their properties are significantly different from the other two classes, and the flux density limit of the VLA survey has a less direct impact on the minimum SFR detectable in these objects (see Section 7).

8.1 SF in RL AGNs

RL AGNs are generally thought to be hosted in massive red and dead galaxies. Indeed, the majority (56 per cent) of our RL AGNs

are hosted in passive galaxies but a significant fraction of them are in MS SFGs and a small fraction (5 per cent) is even hosted in SB systems. Examples of powerful RL AGNs hosted in SB galaxies have been found at high redshift ($z > 3$; e.g. Ivison et al. 2012). We have investigated whether the fraction of actively star-forming host galaxies increases with redshift. As shown in the left-hand panel of Fig. 6, we find no significant trend up to $z \sim 3$. However, we see a strong trend with the stellar mass of the host (see the left-hand panel of Fig. 7). Passive galaxies are the vast majority of RL AGN hosts at masses $> 10^{10.5} M_{\odot}$, while at lower masses they are mostly MS galaxies. This trend is similar to what is observed in the overall galaxy population; the fraction of active galaxies increases as the stellar mass decreases (e.g. Ilbert et al. 2010, 2013; Peng et al. 2010). Therefore, it seems that there is no strong connection between the presence of radio jets and the SF activity of the host. On the other hand, we observe a large spread in stellar masses at low radio power, while the most powerful RL AGNs are only found in the most massive objects (see Fig. 8) suggesting a link between the maximal energy that could be released by the jet and the mass of the BH, assuming the $M_{\text{BH}}-M_{\text{bulge}}$ relation. That could also explain why in shallower radio surveys the fraction of RL AGN hosted in actively star-forming systems is generally lower than what we observe. As our sources are selected in the radio, it is very unlikely that we are missing bright radio sources with small stellar mass. Finally, it is also unlikely that we are simply misclassifying SFGs as RL AGNs since these objects are clear outliers from the RFC, suggesting that there is indeed a significant radio emission associated with jets from the central BH.

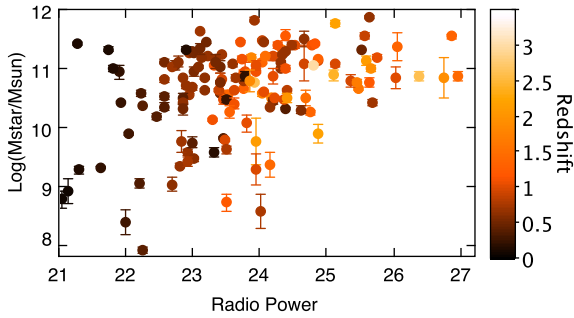


Figure 8. Stellar mass versus radio power for RL AGNs. The colour map shows the redshift of the sources.

8.2 SF in RQ AGNs and SFGs

Once the contribution from RL AGNs is removed, a deep radio survey, as the one presented in this work, can be used to study the SFG population, its distribution in sSFR, and its evolution with redshift. Moreover, we have shown that we can use the radio as an SFR tracer also for the hosts of most RQ AGNs, including sources in which the AGN emission dominates over the stellar emission in the UV, optical, or X-ray bands. This allows for a more complete census of SFGs and permits us to study the AGN contribution in the SFG population.

Our VLA survey is one of the deepest radio surveys available but still it is strongly affected by our flux density limit that, as described in Section 7, allows us to detect the bulk of the SFG population only in the local Universe. Therefore, it is important to carefully take into account selection effects when drawing any conclusion. In this context, a comparison with a mass selected catalogue can be useful. We used a mass selected mock catalogue (Bernhard et al. 2014) of SFGs based on the empirical model for the SFG population described in Sargent et al. (2012) and Béthermin et al. (2012). We will now briefly describe the model and the mock catalogue before continuing with the analysis of the SF properties of our radio selected SFGs and RQ AGNs.

8.2.1 Mock catalogue description

The two basic ingredients to build the mock catalogue are (i) a description of the observed SFG mass function (MF) and its redshift evolution; (ii) a prescription to associate an SFR with each source. For the MF we adopt a parametrization similar to the one used in Sargent et al. (2012), based on the results of Peng et al. (2010) and Ilbert et al. (2010, see Appendix A for more details). This allows us to build a mass selected SFG catalogue down to a stellar mass of $10^7 M_{\odot}$ (which is smaller than the minimum mass measured in our sample) for a mock observation on an area equal to the size of our field (0.285 deg^2).

An SFR is then assigned to each source in order to reproduce the observed MS of SFGs with its redshift evolution (e.g. Daddi et al. 2007; Elbaz et al. 2007; Peng et al. 2010; Rodighiero et al. 2011), and the distribution of sSFR at a fixed stellar mass. The latter is modelled as the sum of two Gaussian components (Sargent et al. 2012), one associated with MS galaxies and the second with SBs. The full width at half-maximum (FWHM) of the two Gaussians, the relative contribution of the two components, and its evolution with redshift are free parameters. We refer to Sargent et al. (2012) and Béthermin et al. (2012) for a better description of this model and to Appendix A for an illustration of the model parameters adopted in this work.

In order to directly compare this mock catalogue with our radio sample, we need to ‘observe’ it with the same flux density limit of our VLA survey. To do that, we converted the SFR of the sources in the mock catalogue to the corresponding radio power according to equation (3), adding a 0.2 dex random scatter, in agreement with what we measure (see Section 4). We then computed the corresponding radio flux density given the source redshift and selected only objects with radio flux densities above $37 \mu\text{Jy}$, the average flux density limit of our VLA survey. Finally, we added random uncertainties with 0.2 dex dispersion on the mass and SFR of the mock objects to take into account the uncertainties affecting real measurements.

Sources in the mock catalogue are flagged as SB or MS object depending on which of the two Gaussian components they belong to. Recovering this information in real observations is not possible for individual sources, but only statistically. Therefore, to compare the SB fraction and its dependence on physical parameters (e.g. stellar mass or radio power) in the mock catalogue and in our sample, we will adopt the same definition of SB, MS, and passive based on the distance of the source from the MS as defined in Section 8. Note that even if the mock catalogue includes in principle only active galaxies, due to the errors we added to the mock catalogue quantities and to the wings of the MS Gaussian distribution, some sources in the mock catalogue are ‘passive’ according to our definition. We also note that, as the RL AGNs are mainly hosted in passive galaxies, the mock catalogue can be used for a comparison with the properties of SFGs and RQ AGNs, where the radio emission traces the SF activity.

8.2.2 SB contribution

In our observed VLA sample, the large majority of SFGs and RQ AGNs are MS objects (~ 74 per cent). The remaining sources are mainly SBs (~ 22 per cent) with a small contribution from passive galaxies (~ 4 per cent; see also Fig. 5). The total observed fraction of SB ($f_{\text{SB,obs}}$) is slightly larger in RQ AGNs compared to SFGs (25 per cent versus 20 per cent). We emphasize that these fractions refer to our radio flux-limited sample, and should not be confused with fractions for a mass selected sample. This result echoes what found for an FIR selected sample by Gruppioni et al. (2013).

In more detail, we can follow $f_{\text{SB,obs}}$ as a function of stellar mass for the two classes of sources (middle panels in Fig. 7). For both SFGs and RQ AGNs, $f_{\text{SB,obs}}$ decreases quickly with increasing stellar mass as at low masses we are highly biased towards high sSFR due to our flux density limit. The behaviour in RQ AGNs is even more extreme and the SB galaxies become the majority at masses smaller than $\sim 10^{10.5} M_{\odot}$. This is mainly due to the fact that we are able to detect low-mass objects only at low redshift (see the first panel of Fig. 5), but, since the volume that we probe at $z < 0.5$ is small, the chance of detecting AGNs is very low. We are able to sample the MS at low masses only for more numerous objects as the SFGs. The effect of the flux density limit becomes clearer looking at the right-hand panel of Fig. 7; we show the SB and MS galaxies’ relative fraction for the mass selected mock catalogue (light colours and open symbols) and for the same sample after applying the flux density cut (dark colours and filled symbols). In the mass selected case, the SB fraction is constant with stellar mass, while the ‘observed’ mock catalogue shows the same trend as in the real VLA samples.

More interestingly, we can also follow the evolution of $f_{\text{SB,obs}}$, that is equivalent to the relative SB contribution to the SFR density,

as a function of redshift. Some hydrodynamic simulations suggest an increase of the SB fraction out to $z \sim 2$ due to the increase of the merger-induced SF at high redshift (e.g. Hopkins et al. 2010). In our VLA sample, we observe a fast growth from the local Universe up to $z \sim 1$ followed by a flattening both for RQ AGNs and SFGs (see the middle panels of Fig. 6). This is not only a consequence of our flux density limits but also reflects the intrinsic growth of the SB contribution from the local Universe to the peak of the SF activity.

Again, the comparison with the mock catalogue allows us to better quantify our results. The evolution of the fraction of SB in a mass selected sample ($f_{\text{SB, mass}}$) is one of the ingredients of the empirical model used to build the mock catalogue (see Appendix A), and we can therefore use our observation to constrain the model parameters. We fixed the local value of $f_{\text{SB, mass}}$ to 1.2 per cent as computed by Sargent et al. (2012) as our small field does not allow us to have enough volume to properly constrain it, while varying the slope of the growth and the redshift above which the evolution stops. We find that a growth as $(1+z)^2$ up to $z = 1$ of $f_{\text{SB, mass}}$ and constant thereafter is required to match the total $f_{\text{SB, obs}}$ in our combined sample of SFGs and RQ AGNs and to reproduce its behaviour as a function of redshift (see Fig. 6).

In summary, the ‘observed’ mock sample reproduces well the behaviours of the relative fraction of SB, MS, and passive galaxies in our SFGs, both as a function of redshift and stellar mass (see the last two panels of Figs 6 and 7, respectively). We note that also when combining SFGs and RQ AGNs, which are the minority in number, the fraction of SB as a function of stellar mass and redshift is consistent with the model within the uncertainties. Also the total $f_{\text{SB, obs}}$ is the same in the VLA and mock flux-limited samples (~ 20 per cent). Therefore, we conclude that the empirical model of Sargent et al. (2012) is suitable to describe the SFG populations with only a little tuning of the model parameters.

Therefore, we could use the model prediction to study the behaviour of a mass selected sample rather than a flux-limited one. In the last panels of both Figs 6 and 7, we show in light colours and open symbols the fraction of SB and MS galaxies for the mass selected catalogue. As expected, the ‘real’ $f_{\text{SB, mass}}$ is much lower compared to the one observed in a flux-limited sample and SB sources contribute to less than 10 per cent to the total SFR density. This result is also in agreement with the results of Rodighiero et al. (2011) and the models of Hopkins et al. (2010).

8.3 AGN content as a function of sSFR

In Fig. 9, we plot the relative fraction of the different classes of sources as a function of the distance with respect to the MS (i.e. $\Delta \log(\text{sSFR})_{\text{MS}} = \log[\text{sSFR}(\text{galaxy})/\text{sSFR}_{\text{MS}}(M_{\text{star}}, z)]$). Below the MS (left side of Fig. 9), the population is dominated by RL AGNs. This is due to two main reasons. The first is related to selection effects since we are sensitive to low sSFR only for sources whose radio emission is enhanced by AGN activity, i.e. RL AGNs. On the other hand, the probability of hosting an RL AGN has been observed to be higher in massive passive galaxies (e.g. Best et al. 2005) even if its physical reason is still unclear.

On the right side of the plot, i.e. above the MS, we observe a rising of the RQ AGN fraction from ~ 25 to 40 per cent. To investigate if this rising can be due to some AGN selection effects, we considered two SFG sub-samples matched in redshift and mass with the RQ AGN distributions. The trend remains in both cases. We also checked if it can be explained by some AGN contribution to the FIR luminosity in two ways: (i) using the SFR derived from the radio power rather than SFR_{FIR} and (ii) using the SFR_{FIR} corrected for

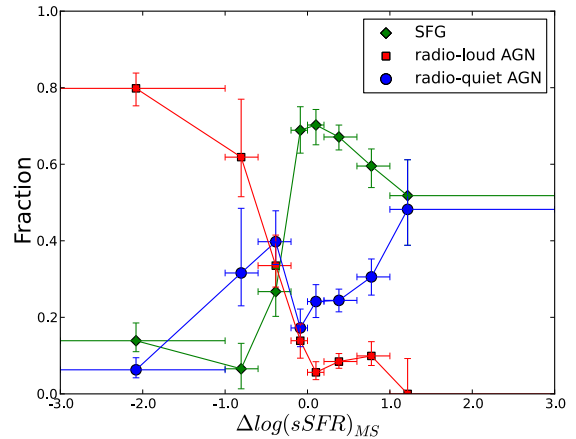


Figure 9. Relative fraction of source classes as a function of $\Delta \log(\text{sSFR})_{\text{MS}}$.

the AGN contribution (as described in Section 6.1) to compute the $\Delta \log(\text{sSFR})_{\text{MS}}$. Again the fraction of RQ AGNs increases as the $\Delta \log(\text{sSFR})_{\text{MS}}$ increases. This result is also in agreement with what found by Gruppioni et al. (2013), who considered an FIR selected sample and found that SB sources are dominated by galaxies with AGN-type SEDs. We will further expand on this result in an upcoming paper (Padovani et al., in preparation). The most extreme SF activity seems to be therefore often associated with an active phase of the BH. Such a scenario has been predicted by simulation of merging systems (e.g. Di Matteo, Springel & Hernquist 2005; Hopkins et al. 2008); the instabilities generated by such a violent event trigger both a burst in the SF and feed efficiently the central BH.

As discussed in the previous section, sources with SB activity represent a small fraction of the SFG population. Similarly, the large majority of our RQ AGNs (75 per cent) are hosted in MS or passive galaxies. This fraction only represents a lower limit since our observations do not fully sample the MS especially at high redshift. Hence, the most common triggering mechanism of the BH activity is probably related to steady process like gas inflows from the intergalactic medium rather than extreme events like major mergers (e.g. Mainieri et al. 2011; Rosario et al. 2012).

9 DISCUSSION

We find that radio power is a tracer for the SFR as good as the FIR luminosity not only for SFGs, but also for RQ AGNs. Hence, our finding suggests that radio emission in RQ AGNs is mainly due to SF. As already mentioned in Section 6, even if some level of correlation between the radio and FIR luminosity was expected due to the fact that RQ AGNs lie in the same locus as SFGs in the $q_{24\text{obs}}$ -redshift plane, the small scatter we find, of only 0.23 dex, was not foreseeable. Indeed, in the MIR, which we use to separate the RL AGNs (see Section 2.2), the AGN contribution can be strong leading to a scatter in $q_{24\text{obs}}$ values for RQ AGNs two times larger compared to SFGs. Nevertheless, we have shown that using only two bands, the radio (1.4 GHz) and the MIR band (24 μm), we can efficiently and with few outliers separate sources powered by the two different radio emission mechanisms, namely jets and SF. Since the UV-optical and also the MIR emission can be heavily contaminated by the AGN emission in powerful AGN, like most of our RQ objects, the radio power could provide a better estimate of the SF in their host galaxy compared to e.g. UV-based tracers. This

result can be particularly useful especially for deep radio surveys without enough FIR coverage. In addition, being radio frequencies almost unaffected by dust extinction, it is suitable for both type I and type II AGNs.

Hypothetically, the good agreement between SFR_r and SFR_{FIR} for RQ AGNs could be the result of a conspiracy where the contribution to the radio luminosity from small jets is exactly compensated by an extra contribution in the FIR. This will boost both the SFR estimates by the same amounts. With the current resolution of the VLA data, we cannot exclude the presence of jets in the centre of these AGNs (e.g. Giroletti & Panessa 2009), and higher resolution radio observations with the VLBI would be needed to spatially resolve them.

9.1 Comparison with an FIR selected sample

We want to investigate the possibility of using deep radio surveys as a useful tool to study the cosmic SF history, alternative or complementary to FIR surveys. We have therefore compared our sample with the *Herschel*/PACS detected sample.

As described in Section 2.3, only ~ 60 per cent of our VLA sample has a counterpart in the *Herschel* catalogue of the E-CDFS. Excluding the RL AGNs, for which we expected a low detection rate as most of them are hosted in passive galaxies (but see Section 8.1), the fraction increases to ~ 70 per cent. As for the 30 per cent of unmatched radio sources, this is at least partly due to the dispersion of the RFC: a radio and an FIR flux density-limited sample would tend to be biased towards sources on opposite sides of the relation. To test this hypothesis, we made use of the mass selected mock catalogue described in Section 8.2.1. We ‘observed’ it with an FIR luminosity limit equivalent to our $37 \mu\text{Jy}$ flux density limit computing the minimum SFR corresponding to the radio flux density limit at each source redshift and selecting only the objects with SFR above this threshold. The resulting FIR selected catalogue contains ~ 780 sources, roughly the same number of objects as in the radio selected mock catalogue described in Section 8.2.1. In Fig. 10 we show the RFC for the FIR selected mock catalogue in cyan, the radio selected in magenta, and for the matched sources, in blue. The latter are only 60 per cent of the total number of objects in each catalogue, a fraction similar to the one obtained matching the real VLA and *Herschel* samples. The offset from the 1:1 correlation is ~ 0.15 dex above and below for the FIR and radio selected samples, respectively. This plot also explains why most of the VLA sources without PACS detection are just below the correlation found for the VLA sources with *Herschel* counterpart in Fig. 3: being radio detected only when they have a slight radio excess.

On the other hand, about 40 per cent of the PACS detected sources have a counterpart in the VLA image. This means that the FIR observations reach a lower flux density limit, also thanks to the much deeper maps in the central GOODS field compared to the outskirts (see Section 2.3). We have compared the SFR_{FIR} computed in Gruppioni et al. (2013) for the sources in common and we find very good agreement with our estimates. Also the stellar masses are consistent; we find a larger scatter but no systematic shifts. This reflects the fact that the SFR is well constrained when FIR photometry is available, while on the stellar masses there are larger uncertainties, especially in AGN host galaxies, depending on the fitting technique and especially on the model library adopted (e.g. Ilbert et al. 2010).

In Fig. 11, we show the VLA (RQ AGNs and SFGs only) and the *Herschel* samples on the SFR–stellar mass plane with the sources coloured according to their redshift. The two sets of data show the

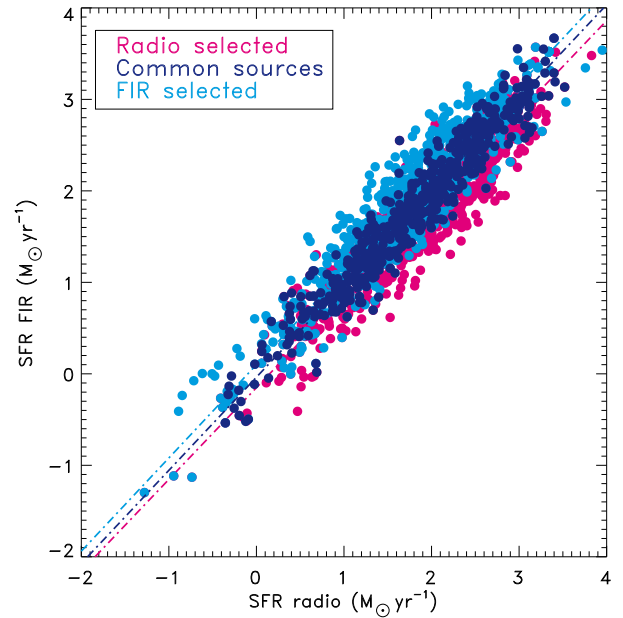


Figure 10. SFR derived from the FIR luminosity versus the SFR from the radio luminosity for the sources in the FIR selected mock catalogue (cyan), the radio selected mock catalogue (magenta) and the matched sample (blue). The dashed lines are the linear fit to the data.

same trends and the same evolution with redshift. We also find a similar fraction of SB (20 per cent) in the PACS sample compared to the radio one. Being a bit deeper, especially in the GOODS field, the PACS observations probe better the small stellar mass end and are able to detect more low-SFR sources at low redshift. Already ongoing deeper radio surveys, as well as those planned with future facilities, will allow us to probe these small masses also in the radio (Norris et al. 2013). Indeed, going down to the nanoJy sensitivity level, they will be able to probe the bulk of the SFGs population. An illustration of that is given in Fig. 12 where we plot the fractions of MS and SB galaxies as a function of the radio flux density in μJy for the mass selected mock catalogue. Below about $10 \mu\text{Jy}$, the number density of SB remains nearly constant around 8 per cent, while at the flux density limit of our survey (vertical line) we are biased towards higher sSFRs.

9.2 What changes using a different SFR tracer?

As discussed in the previous section, due to the RFC dispersion, a sample selected with a radio flux density limit would be slightly biased towards those objects on the right side of the relation, i.e. with a radio power larger than the one given by the relation for a given FIR luminosity.

That means that, especially for the sources without *Herschel* counterpart, the SFR derived from the two different tracers can be slightly different. As quantities like the fraction of SB are extremely sensitive to these changes due to small number statistics, we investigated how the choice of a different SFR tracer, namely the radio power, can affect our conclusions. Of course that cannot be done for RL AGNs as in these objects the radio power is not tracing the SF activity in the host galaxy but it is highly contaminated by the jet emission. For RQ AGNs and SFGs instead, we repeated the same analysis as in Section 8 using the SFR_r to

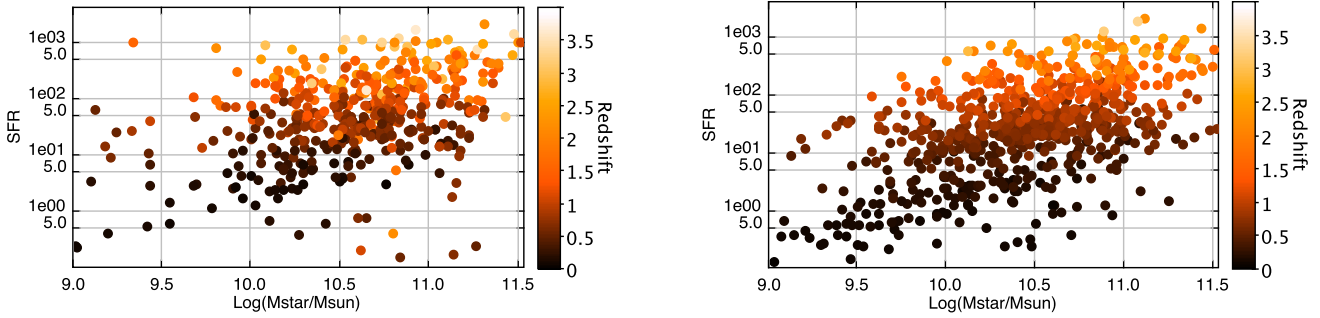


Figure 11. SFR versus stellar mass for the VLA sample (left) and for the PACS sample (right).

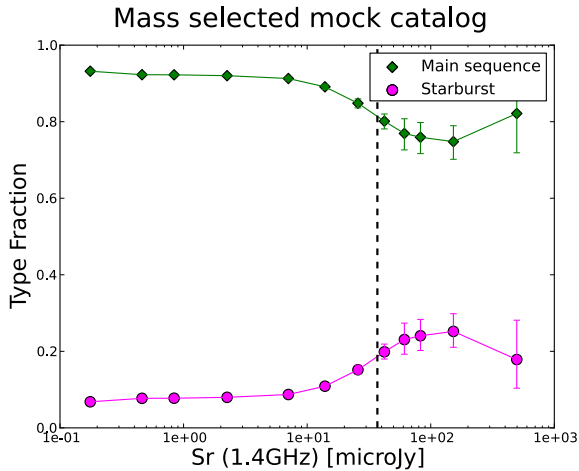


Figure 12. Fraction of MS and SB sources in the mass selected mock catalogue as a function of the radio flux density.

compute the $\Delta \log(\text{sSFR})_{\text{MS}}$ and therefore to determine the level of their SF activity.

The total fraction of SB in this radio flux-limited sample increases to ~ 30 per cent⁴ but the trends as a function for example of stellar masses remain the same (see Fig. 13). Also in the radio flux density-limited mock catalogue, if we compute the $\Delta \log(\text{sSFR})_{\text{MS}}$ from their radio power, we obtain an $f_{\text{SB,obs}}$ of 30 per cent, in agreement with our data.

The larger differences appear at $z > 1$, where the fraction of SBs is up to a factor of 2 larger using the SFR_r , but this effect is mainly due to the sources without PACS detection. Indeed, as shown in Fig. 4, the SFR extrapolated from the optical-to-MIR photometry tends to be underestimated at high redshift. Hence, the differences between the two SFR tracers appear larger. As a further consequence, the $f_{\text{SB,obs}}$ at high redshift shown in the central panels of Fig. 6 are slightly underestimated as also suggested by the predictions of the empirical model.

9.3 L_X - L_{FIR} relation

The hard band X-ray luminosity (L_X) is considered another SFR tracer up to high redshift (Norman et al. 2004). In SB galaxies the 2–10 keV rest-frame emission is dominated by high-mass X-ray binaries. Being the companion of the accreting object, a short-lived high-mass star's L_X is linked to the recent SF activity. At

low SFRs, however, there is contamination from low-mass X-ray binaries which do not trace the immediate SFR due to their long evolution lifetimes. The conversion factor between L_X and the SFR has been calibrated for local samples (e.g. Ranalli, Comastri & Setti 2003; Persic et al. 2004; Lehmer et al. 2012). It has been argued that the hard band X-ray luminosity can be used as an unbiased SFR indicator up to high redshifts, despite the contamination from obscured AGN which may be unnoticed in distant, faint sources.

Recently, Vattakunnel et al. (2012) used the deep X-ray *Chandra* data (total integration time of 4 Ms; see Xue et al. 2011; Lehmer et al. 2012) and the deep VLA observation (Miller et al. 2013) to explore the L_X - P_r relation in galaxies dominated purely by SF processes in both bands. Due to the strict selection process, aimed at discarding any significant AGN contamination, they obtained a sample of 43 SFGs up to $z \sim 1.2$. They found a clear linear correlation between radio and X-ray luminosity in SFGs over three orders of magnitude in this redshift range, consistent with that measured locally. They also measured a significant scatter of the order of ~ 0.4 dex, higher than that observed at low redshift, implying an intrinsic scatter component, or some residual AGN contamination.

The information on the IR properties of the E-CDFS sources presented in this work allows us to further explore the relation between L_X and SFR in this sub-sample of sources. As a first step, we consider only 35 sources, out of 43, which have a $> 5\sigma$ radio detection, and plot the $L_{\text{FIR}}-P_r$ relation. We find that the bulk of the sources follow the radio-infrared correlation expected for SFGs (see Fig. 14, left-hand panel), confirming that the selection was effective in selecting sources powered by SF processes. However, we find four clear outliers at low IR luminosities, which indeed were classified as RL AGNs according to their $q_{24\text{obs}}$ value (see Bonzini et al. 2013, for details). For the remaining 31 sources, we plot the L_X-L_{FIR} relation (see Fig. 14, right-hand panel).

We also measure the observed scatter in the L_X-L_{FIR} and $L_{\text{FIR}}-P_r$ relations finding that in the first case the dispersion is ~ 0.29 dex, about two times larger than the scatter of the $L_{\text{FIR}}-P_r$ relation (0.17 dex). Even after removing the statistical error associated with the X-ray and radio luminosity, the intrinsic scatter of the L_X-L_{FIR} relation remains two times larger than the other. Given the robust selection, we can safely assume negligible AGN contamination, and therefore interpret this scatter as an intrinsic scatter associated with the SFR tracer. Therefore, for the first time we show that the X-ray luminosity, as an SFR tracer, is noisier than radio and IR luminosities.

The scatter can be due to an increasing X-ray emission component proportional to the stellar mass and not to the instantaneous SFR, analogous to what has been found in a sample of luminous infrared galaxies by Lehmer et al. (2010). Alternatively, the scatter may be due to the hard component of a strongly absorbed AGN component.

⁴ Note that, in contrast, the fraction of passive goes almost to zero.

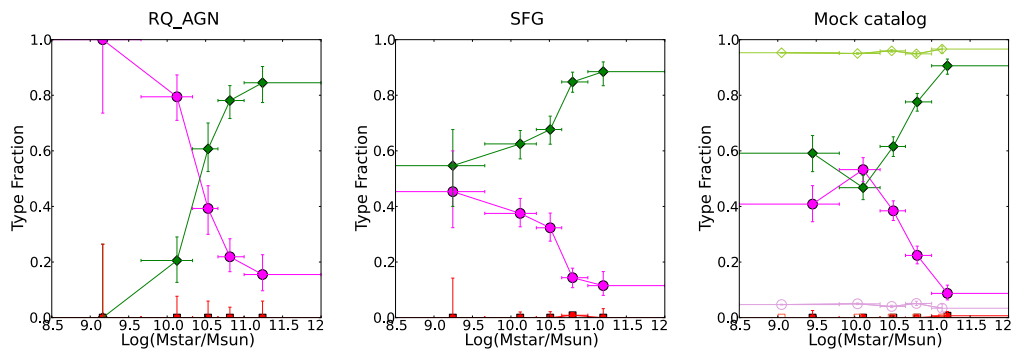


Figure 13. Fraction of SB (magenta circles), MS galaxies (green diamonds), and passive galaxies (red squares) derived using the SFR_r , versus stellar mass. The panels refer from left to right to RQ AGNs, SFGs, and mock catalogue sources.

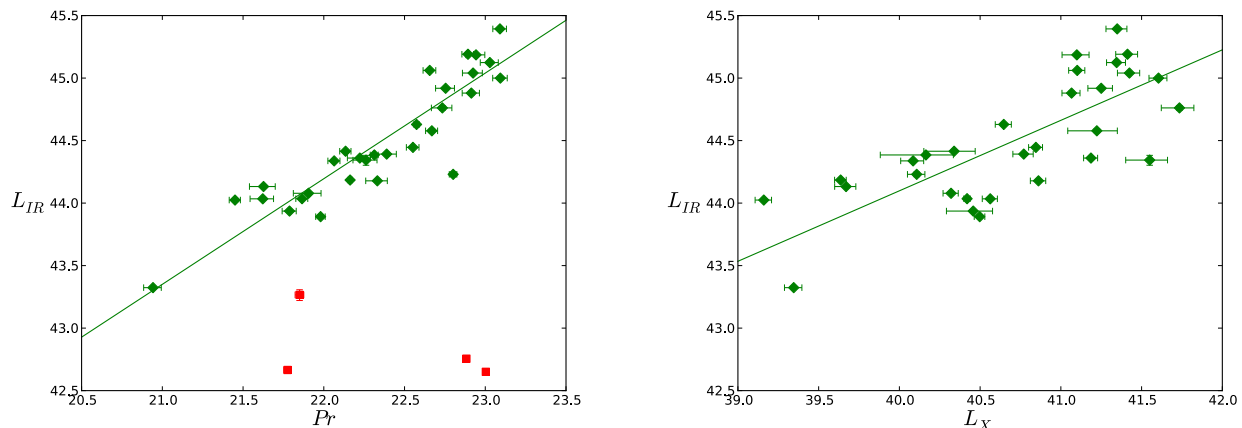


Figure 14. Left: P_r - L_{IR} relation for the sub-sample of SFGs with X-ray counterpart selected in Vattakunnel et al. (2012). The four sources classified as RL AGNs in Bonzini et al. (2013) are plotted as red squares. Right: L_X - L_{IR} relation for the same sub-sample after removing the outliers in the P_r - L_{IR} relation.

10 SUMMARY

In this work, we investigated the SF properties of the faint radio population as detected by one of the deepest 1.4 GHz survey up-to-date conducted with the VLA in the E-CDFS. This study builds upon the results presented in Bonzini et al. (2012, 2013) where we have exploited the wealth of multiwavelength data available in this field to identify the AGNs, further divide them into RL and RQ, and characterize the properties of the radio selected galaxies (e.g. redshift, stellar mass). The main results of this paper are the following.

(i) We have derived the FIR luminosity, fitting the UV-to-FIR SED of our VLA sources; radio selected SFGs follow the RFC up to $z \sim 3$ with a nearly constant dispersion of 0.2 dex (Section 4).

(ii) Comparing the SFR derived from the FIR luminosity and the radio power (Table B1), we show that the two SFR tracers are equivalently good not only in non-active SFGs but also for the host galaxies of RQ AGNs. This implies that the main contribution to the radio emission in RQ AGNs (at least at $z \sim 1.5$ –2) is associated with SF activity in the host rather than with radio jets (if present) powered by the BH (Section 6).

(iii) As the SFR in SFGs correlates with their stellar mass, we made use of the sSFR to determine the SF activity level in our sample (Section 8). The data are consistent with models that predict that the SB galaxies represent a small fraction (~ 8 per cent) of a mass selected SFG population (e.g. Béthermin et al. 2012; Sargent et al. 2012). We have also discussed the impact of our flux density limit on a mass selected mock catalogue (Section 8.2).

(iv) The majority of our RL AGNs are hosted in passive galaxy, but we detect significant SF activity in ~ 40 per cent of the RL AGN hosts. This suggests that, at least for low radio power, the presence of radio jets does not always prevent active SF (Section 8.1).

(v) We find hints of a higher fraction of AGNs in the most extreme SB galaxies (Section 8.3). This is in agreement with scenarios where both the intense SF activity and the efficient accretion on the BH are triggered by gas-rich major mergers (e.g. Chen et al. 2013; Symeonidis et al. 2013).

(vi) The vast majority (~ 75 per cent) of our RQ AGNs lie along the MS suggesting that the bulk of the BH activity is associated with secular processes.

Finally, we have shown that deep radio continuum surveys are a powerful tool to investigate the SF history up to high redshift. The current and upcoming radio facilities like the Jansky Very Large Array (JVLA) and the Square Kilometre Array pathfinders will be able to observe with nanoJy (1σ) sensitivity large areas of the sky (Norris et al. 2013), hence detecting the bulk of the SF population. Therefore, our finding that the main contribution of radio emission in RQ AGNs is due to SF in their host galaxy opens the possibility to use radio emission to estimate the SFR even in the host galaxy of bright quasars.

ACKNOWLEDGEMENTS

This work is based on observations with the National Radio Astronomy Observatory which is a facility of the National Science

Foundation operated under cooperative agreement by Associated Universities, Inc.

PACS has been developed by a consortium of institutes led by MPE (Germany) and including UVIE (Austria); KU Leuven, CSL, IMEC (Belgium); CEA, LAM (France); MPIA (Germany); INAF-IFSI/OAA/OAP/OAT, LENS, SISSA (Italy); IAC (Spain). This development has been supported by the funding agencies BMVIT (Austria), ESA-PRODEX (Belgium), CEA/CNES (France), DLR (Germany), ASI/INAF (Italy), and CICYT/MCYT (Spain).

REFERENCES

- Appleton P. N. et al., 2004, *ApJS*, 154, 147
 Bell E. F., 2003, *ApJ*, 586, 794
 Bernhard E., Béthermin M., Sargent M., Buat V., Mullaney J. R., Pannella M., Heinis S., Daddi E., 2014, *MNRAS*, 442, 509
 Berta S. et al., 2013, *A&A*, 551, A100
 Best P. N., Kauffmann G., Heckman T. M., Brinchmann J., Charlot S., Ivezić Ž., White S. D. M., 2005, *MNRAS*, 362, 25
 Béthermin M., Dole H., Beelen A., Aussel H., 2010, *A&A*, 512, A78
 Béthermin M. et al., 2012, *ApJ*, 757, L23
 Bonzini M. et al., 2012, *ApJS*, 203, 15
 Bonzini M., Padovani P., Mainieri V., Kellermann K. I., Miller N., Rosati P., Tozzi P., Vattakunnel S., 2013, *MNRAS*, 436, 3759
 Cardamone C. N. et al., 2010, *ApJS*, 189, 270
 Chabrier G., 2003, *PASP*, 115, 763
 Chen C. T. J. et al., 2013, *ApJ*, 773, 3
 Ciliegi P., Zamorani G., Hasinger G., Lehmann I., Szokoly G., Wilson G., 2003, *A&A*, 398, 901
 Condon J. J., 1992, *ARA&A*, 30, 575
 Daddi E. et al., 2007, *ApJ*, 670, 156
 Daddi E. et al., 2010a, *ApJ*, 713, 686
 Daddi E. et al., 2010b, *ApJ*, 714, L118
 Damen M. et al., 2011, *ApJ*, 727, 1
 de Jong T., Klein U., Wielebinski R., Wunderlich E., 1985, *A&A*, 147, L6
 Del Moro A. et al., 2013, *A&A*, 549, A59
 Di Matteo T., Springel V., Hernquist L., 2005, *Nature*, 433, 604
 Dickey J. M., Salpeter E. E., 1984, *ApJ*, 284, 461
 Dickinson M., FIDEL Team, 2007, *BAAS*, 39, 822
 Diolaiti E., Bendinelli O., Bonaccini D., Close L., Currie D., Parmeggiani G., 2000a, *A&AS*, 147, 335
 Diolaiti E., Bendinelli O., Bonaccini D., Close L. M., Currie D. G., Parmeggiani G., 2000b, in Wizinowich P. L., ed., *Proc. SPIE*, Vol. 4007, Adaptive Optical Systems Technology. SPIE, Bellingham, p. 879
 Donley J. L., Rieke G. H., Rigby J. R., Pérez-González P. G., 2005, *ApJ*, 634, 169
 Donley J. L. et al., 2012, *ApJ*, 748, 142
 Drake C. L., McGregor P. J., Dopita M. A., van Breugel W. J. M., 2003, *AJ*, 126, 2237
 Elbaz D. et al., 2007, *A&A*, 468, 33
 Elbaz D. et al., 2011, *A&A*, 533, A119
 Genzel R. et al., 2010, *MNRAS*, 407, 2091
 Giroletti M., Panessa F., 2009, *ApJ*, 706, L260
 González V., Bouwens R., Illingworth G., Labbé I., Oesch P., Franx M., Magee D., 2014, *ApJ*, 781, 34
 Gruppioni C. et al., 2013, *MNRAS*, 432, 23
 Harrison C. M. et al., 2012, *ApJ*, 760, L15
 Hatziminaoglou E. et al., 2010, *A&A*, 518, L33
 Hopkins P. F., Hernquist L., Cox T. J., Kereš D., 2008, *ApJS*, 175, 356
 Hopkins P. F., Younger J. D., Hayward C. C., Narayanan D., Hernquist L., 2010, *MNRAS*, 402, 1693
 Ilbert O. et al., 2010, *ApJ*, 709, 644
 Ilbert O. et al., 2013, *A&A*, 556, A55
 Ivison R. J. et al., 2010, *A&A*, 518, L31
 Ivison R. J. et al., 2012, *MNRAS*, 425, 1320
 Kennicutt R. C., Jr, 1998, *ARA&A*, 36, 189
 Lacki B. C., Thompson T. A., 2010, *ApJ*, 717, 196
 Lacki B. C., Thompson T. A., Quataert E., 2010, *ApJ*, 717, 1
 Lehmer B. D., Alexander D. M., Bauer F. E., Brandt W. N., Goulding A. D., Jenkins L. P., Ptak A., Roberts T. P., 2010, *ApJ*, 724, 559
 Lehmer B. D. et al., 2012, *ApJ*, 752, 46
 Lutz D., 2014, *Ann. Rev. Astron. Astrophys.*, 52, 373
 Lutz D. et al., 2011, *A&A*, 532, A90
 Magnelli B. et al., 2012, *A&A*, 539, A155
 Magnelli B. et al., 2013, *A&A*, 553, A132
 Mainieri V. et al., 2011, *A&A*, 535, A80
 Mauch T., Sadler E. M., 2007, *MNRAS*, 375, 931
 Miller P., Rawlings S., Saunders R., 1993, *MNRAS*, 263, 425
 Miller N. A., Fomalont E. B., Kellermann K. I., Mainieri V., Norman C., Padovani P., Rosati P., Tozzi P., 2008, *ApJS*, 179, 114
 Miller N. A. et al., 2013, *ApJS*, 205, 13
 Morić I., Smolčić V., Kimball A., Riechers D. A., Ivezić Ž., Scoville N., 2010, *ApJ*, 724, 779
 Mullaney J. R. et al., 2012, *MNRAS*, 419, 95
 Noeske K. G. et al., 2007, *ApJ*, 660, L43
 Norman C. et al., 2004, *ApJ*, 607, 721
 Norris R. P. et al., 2013, *PASA*, 30, e020
 Padovani P., Mainieri V., Tozzi P., Kellermann K. I., Fomalont E. B., Miller N., Rosati P., Shaver P., 2009, *ApJ*, 694, 235
 Padovani P., Miller N., Kellermann K. I., Mainieri V., Rosati P., Tozzi P., 2011, *ApJ*, 740, 20
 Padovani P., Bonzini M., Kellermann K. I., Miller N., Mainieri V., Tozzi P., 2015, *MNRAS*, 452, 1263
 Page M. J. et al., 2012, *Nature*, 485, 213
 Pannella M. et al., 2009, *ApJ*, 698, L116
 Peng Y. j. et al., 2010, *ApJ*, 721, 193
 Persic M., Rephaeli Y., Braitto V., Cappi M., Della Ceca R., Franceschini A., Gruber D. E., 2004, *A&A*, 419, 849
 Polletta M. et al., 2007, *ApJ*, 663, 81
 Rafferty D. A., Brandt W. N., Alexander D. M., Xue Y. Q., Bauer F. E., Lehmer B. D., Luo B., Papovich C., 2011, *ApJ*, 742, 3
 Ranalli P., Comastri A., Setti G., 2003, *A&A*, 399, 39
 Rodighiero G. et al., 2011, *ApJ*, 739, L40
 Rosario D. J. et al., 2012, *A&A*, 545, A45
 Santini P. et al., 2009, *A&A*, 504, 751
 Sargent M. T. et al., 2010, *ApJS*, 186, 341
 Sargent M. T., Béthermin M., Daddi E., Elbaz D., 2012, *ApJ*, 747, L31
 Schleicher D. R. G., Beck R., 2013, *A&A*, 556, A142
 Smolčić V. et al., 2008, *ApJS*, 177, 14
 Sopp H. M., Alexander P., 1991, *MNRAS*, 251, 14p
 Stark D. P., Schenker M. A., Ellis R., Robertson B., McLure R., Dunlop J., 2013, *ApJ*, 763, 129
 Symeonidis M. et al., 2013, *MNRAS*, 433, 1015
 Taylor E. N. et al., 2009, *ApJS*, 183, 295
 Vattakunnel S. et al., 2012, *MNRAS*, 420, 2190
 Weinmann S. M., Neistein E., Dekel A., 2011, *MNRAS*, 417, 2737
 Wuyts S. et al., 2011, *ApJ*, 742, 96
 Xue Y. Q. et al., 2011, *ApJS*, 195, 10
 Yun M. S., Reddy N. A., Condon J. J., 2001, *ApJ*, 554, 803
 Zubovas K., Nayakshin S., King A., Wilkinson M., 2013, *MNRAS*, 433, 3079

SUPPORTING INFORMATION

Additional Supporting Information may be found in the online version of this article:

table_properties_full_modified_pz_cov_units
<http://mnras.oxfordjournals.org/lookup/suppl/doi:10.1093/mnras/stv1675/-/DC1>.

Please note: Oxford University Press are not responsible for the content or functionality of any supporting materials supplied by the authors. Any queries (other than missing material) should be directed to the corresponding author for the paper.

APPENDIX A: CHOICE OF THE MODEL PARAMETER

We describe here in more details the empirical model used to build the mock catalogue (Bernhard et al. 2014) and discuss the set of model parameters adopted. The physical motivation for the model and the underlying equations are described in Sargent et al. (2012) and Béthermin et al. (2012).

The motivation for this appendix is that the original set of parameters adopted in Béthermin et al. (2012) needed to be modified in order to reproduce our observations. Indeed, the corresponding mock catalogue, ‘observed’ with the same flux density limit of our survey (see Section 8.2.1), while reproducing approximatively the radio counts, does not well reproduce some host galaxy properties of the sample; the mock catalogue has a mass distribution that peaks at higher masses compared to the distribution for our VLA sources. As a consequence, also the SFR properties are not well reproduced in the mock catalogue having on average lower SFR and therefore a significantly lower fraction of SB galaxies compared to the data.

Therefore, we investigated the possible reasons for this discrepancy and looked for a set of parameters that are able to reproduce our observations in terms of mass and sSFR distribution together with the radio counts.

A1 SFG MF

The mass distribution of the mock catalogue objects is set by the SFG MF. The MF adopted in the model is based on the fits by Peng et al. (2010) of the SFG MF presented in Ilbert et al. (2010). It is described as a single Schechter function with characteristic mass (M_b) and faint-end slope that are redshift invariant and by a constant characteristic density up to $z \sim 1$ followed by a decline as $(1 - z)^{0.46}$ (see Béthermin et al. 2012 for details). Our radio observations are relatively shallow compared to the *K*-band data used to compute the MF in Ilbert et al. (2010); consequently, we are more sensitive to the high-mass end of the distribution. Therefore, we are particularly sensitive to the value of M_b , which sets the position of the MF break followed by the exponential cutoff. Since our sample is small and highly incomplete at low masses, we cannot perform a real fit of the MF. We chose to keep all the other parameters describing the MF fixed. As already mentioned, our observations have a mass distribution that peaks at lower masses compared to the corresponding mock catalogue. To reconcile the model with our observations, we assume an M_b of $10^{11} M_\odot$ rather than $10^{11.2} M_\odot$ as in Béthermin et al. (2012). Adopting this value the mass distributions of the mock catalogue and of our data are consistent as confirmed by a Kolmogorov–Smirnov test (Prob > 0.99). The possible reasons for this shift are twofold: on one hand, stellar mass measurements have large uncertainties and can be up to 0.3 dex systematically different depending on the stellar population synthesis model adopted (see e.g. Ilbert et al. 2010). To check this hypothesis, we computed the stellar mass using the same method adopted for the VLA sources (Bonzini et al. 2013) for a sub-sample of the Ilbert et al. (2010) sources⁵ and compared the mass measurements. We indeed noted that the Ilbert et al. (2010) stellar masses are on average larger than the one obtained with our method. On the other hand, there is no one-to-one correspondence between the colour–colour-based method used to identify the SFG population in Ilbert et al. (2010) and our scheme; it is therefore possible that some

sources excluded from the Ilbert et al. (2010) SFG sample because of their redder colours have been considered SFGs according to our classification. Finally, we note that the simple prescription adopted in the empirical model and the set of parameters chosen are only an approximation for the SFG MF, while a more complex description as e.g. in Ilbert et al. (2013) would be needed.

A2 MS and its redshift evolution

The two modes of SF are described by two Gaussians (Sargent et al. 2012). We assume an FWHM of 0.2 dex for the MS galaxies as measured in Rodighiero et al. (2011). For the second Gaussian, we use the same parameter adopted in Béthermin et al. (2012), i.e. an FWHM of 0.2 dex, a displacement from the MS peak of 0.6 dex. The relative fraction of SB evolves with redshift as

$$f_{\text{SB}} = 0.012 \times (1 + z)^2 \text{ for } z < 1. \quad (\text{A1})$$

The local fraction is taken from Béthermin et al. (2012) but we set a steeper growth of the SB fraction up to redshift 1 as suggested by our observations (see Section 8.2).

The normalization of the MS is another critical parameter in determining both the number counts and the observed SB fraction. Keeping fixed the slope of the MS to the value measured in Rodighiero et al. (2011) and its evolution with redshift to $(1 + z)^{2.8}$ (Sargent et al. 2012), we looked for the best value for the MS normalization. We adopt a normalization of the MS ($\log \text{sSFR}(z = 0, M = 10^{11} M_\odot) = 10.08$) that is lower than that in Béthermin et al. (2010) but it is in better agreement with what was found in Rodighiero et al. (2011) and our own measurement. It is also consistent with previous results in the literature up to $z \sim 2$ (Daddi et al. 2007; Elbaz et al. 2007; Noeske et al. 2007). Recent work suggests that above $z \sim 2$ the evolution of the MS is shallower than $(1 + z)^{2.8}$ as assumed by the Bernhard et al. (2014) model (e.g. Weinmann, Neistein & Dekel 2011; Stark et al. 2013; González et al. 2014). As a consequence, the MS shown in the last panel of Fig. 5 is probably too high. However, only about 5 per cent of our sources fall in this high-redshift bin ($2.5 < z < 4$) and therefore the simplification adopted in the model does not affect significantly our conclusions. We stress that the main goal of the comparison of our data with the mock catalogue was to better quantify the selection effects in flux density-limited samples, to check the qualitative agreement with the two-Gaussian SF mode model (Sargent et al. 2012) and not to obtain a fit of the MS as a function of redshift.

A3 Comparison with VLA observations

With the few changes in the model parameters described above, we are able to reproduce both the radio counts and the physical properties of our radio sources with the mock catalogue. Indeed, the mass selected mock catalogue, ‘observed’ with the same flux density limit of our VLA survey (see Section 8.2.1), on a mock field with the same area of our observation, contains about 790 sources. The exact number of sources varies by some units for different runs of the model since we add random uncertainties on the mock galaxy properties and a random dispersion for the RFC. The VLA sample considered in this work contains 779 sources. Considering only the RQ AGNs and the SFGs, where the main contribution to the radio flux is due to SF, but correcting for the not perfect uniformity of the sky coverage (Padovani et al. 2015), the number of RQ AGNs and SFGs detectable at the 37 μJy flux density limit in our field is 784. Considering that some of the RL AGNs, according to our analysis, contribute to the SFG population, we conclude that the number

⁵ A sample of X-ray selected AGNs for which we have optical-to-24 μm photometry and redshift.

Table B1. SF properties of the VLA sources. (The full table is available in the online journal. A portion is shown here for guidance regarding its form and content.)

(1) ID	(2) Class	(3) Type	(4) z	(5) M_{star} [$\log(M_{\odot})$]	(6) SFR_r [$\log(M_{\odot} \text{ yr}^{-1})$]	(7) SFR_{FIR} [$\log(M_{\odot} \text{ yr}^{-1})$]	(8) sSFR _{ex}	(9) PACS?
711	RL AGN	P	1.89	10.77 ± 0.18	277.9 ± 77.6	4 ± 0.1	-1.30	0
712	SFG	MS	0.56	10.79 ± 0.05	15.4 ± 4.7	21 ± 1.1	0.07	1
713	RQ AGN	MS	0.49	10.60 ± 0.06	17.2 ± 3.3	10 ± 0.8	-0.01	1
714	SFG	MS	0.77	10.30 ± 0.02	41.0 ± 9.3	30 ± 4.0	0.47	1
715	SFG	SB	0.18	9.95 ± 0.07	13.3 ± 0.8	11 ± 0.2	0.81	1
716	RQ AGN	MS	1.16	10.78 ± 0.10	80.2 ± 25.1	79 ± 20.9	0.27	1
717	SFG	MS	0.52	10.13 ± 0.02	17.7 ± 3.8	12 ± 0.9	0.41	1
718	SFG	SB	2.46	10.52 ± 0.09	478.7 ± 141.2	703 ± 86.2	0.84	1
719	RL AGN	MS	1.03	10.84 ± 0.19	$38\,394.1 \pm 20.2$	19 ± 0.2	-0.31	0
720	SFG	MS	0.25	10.59 ± 0.02	16.5 ± 2.4	10 ± 0.5	0.19	1

counts predicted by the empirical model are in good agreement with the observed one. A complete analysis of the impact of the various model parameters on the mock catalogue physical characteristics is beyond the scope of this paper. The goal of this investigation was to check the consistency between our observation and the model for the SF population proposed in Sargent et al. (2012) and to better control the effects of the flux density limit on our results.

APPENDIX B: STELLAR MASSES AND SFR CATALOGUE OF VLA SOURCES

We make publicly available the physical properties derived for our radio sample and used in this work. They are summarized in Table B1. The catalogue columns are organized as follows:

- (1) identification number of the radio source (RID);
- (2) source classification;

(3) source activity: ‘SB’ for starburst galaxies, ‘MS’ for main-sequence galaxies, and ‘P’ for passive galaxies according to the definition given in Section 8;

(4) source redshift;

(5) stellar mass;

(6) SFR derived from the radio power;

(7) SFR derived from the FIR luminosity;

(8) distance with respect to the MS in the $\text{SFR}-M_{\text{star}}$ plane (Section 8.3);

(9) PACS flag: 0 = only upper limits in the PACS bands, 1 = at least one PACS detection.

This paper has been typeset from a $\text{T}_{\text{E}}\text{X}/\text{L}^{\text{A}}\text{T}_{\text{E}}\text{X}$ file prepared by the author.